Nanoscale

PAPER

View Article Online
View Journal | View Issue

Cite this: *Nanoscale*, 2016, **8**, 13280

Three-dimensional nanotube electrode arrays for hierarchical tubular structured high-performance pseudocapacitors†

Yuan Gao,[a] Yuanjing Lin,[a] Jiaqi Chen,[a] Qingfeng Lin,[a] Yue Wu,[a] Wenjun Su,[b] Wenli Wang*[c,d] and Zhiyong Fan*[a]

Received 24th April 2016,
Accepted 3rd June 2016

DOI: 10.1039/c6nr03337g

www.rsc.org/nanoscale

Ordered three-dimensional (3-D) tubular arrays are highly attractive candidates for high performance pseudocapacitor electrodes. Here, we report 3-D fluorine doped tin oxide (FTO) tubular arrays fabricated by a cost-effective ultrasonic spray pyrolysis (USP) method in anodic aluminum oxide (AAO) channels with high uniformity. The large surface area of such a structure leads to remarkable surface area enhancement up to 51.8 times compared to a planar structure. Combining with electrochemically deposited manganese dioxide (MnO_2) nanoflakes on the inner side wall of the FTO nanotubes, the unique hierarchical tubular structured pseudocapacitor electrode demonstrated the highest areal capacitance of 193.8 mF cm^{-2} at the scan rate of 5 mV s^{-1} and 184 mF cm^{-2} at the discharge current density of 0.6 mA cm^{-2}, which is 18.5 times that of a planar electrode. And it also showed a volumetric capacitance of 112.6 F cm^{-3} at the scan rate of 5 mV s^{-1} and 108.8 F cm^{-3} at the discharge current density of 0.6 mA cm^{-2}. In addition, the cyclic stability test also indicated that a nanostructured pseudocapacitive electrode has a much larger capacitance retention after 3000 cycles of the charge–discharge process compared with a planar electrode, primarily due to the mechanical stability of the nanostructure. Moreover, pseudocapacitor device fabrication based on such electrodes shows the volumetric capacitance of 17.5 F cm^{-3}, and the highest specific energy of 1.56×10^{-3} Wh cm^{-3}. With the merit of facile fabrication procedures and largely enhanced electrochemical performance, such a 3-D structure has high potency for energy storage systems for a wide range of practical applications.

Introduction

Driven by the surge of energy consumption in a broad range of applications, such as portable electronics, communication, and transportation, high performance energy storage systems are in urgent need worldwide. As attractive alternatives or complements for electrochemical batteries, supercapacitors have appealing attributes including a much faster charge–discharge rate, higher power density, longer cycle life time, and thus could serve as promising energy back-up in electric vehicles, unmanned aircrafts, micro self-powered systems, *etc.*[1–4] A pseudocapacitor is one type of widely studied supercapacitor with high performance utilizing a surface chemical redox reaction to store electrical charge.[5–8] In such a device, the electrode surface area is one of the key factors determining the performance of the device, besides the intrinsic properties of electrode materials. In this regard, fabrication of nanostructured electrodes has been widely explored, mainly due to the fact that they have a large electrode surface area and thus can significantly improve overall device capacitance.[9–18] Among different nanostructures, ordered three-dimensional (3-D) tubular arrays are regarded as one of the most promising structures as electrochemical electrodes,[19–32] mainly due to the facts that (i) this structure has a large internal surface area for more pseudo-capacitive material deposition;[18,33]

---

[a] *Department of Electronic and Computer Engineering, The Hong Kong University of Science and Technology, Clear Water Bay, Kowloon, Hong Kong, China SAR. E-mail: eezfan@ust.hk*

[b] *School of Mechanical Engineering, Xi'an Jiaotong University, Xi'an, Shaanxi 710049, China*

[c] *College of Textile and Clothing Engineering, Soochow University, Suzhou, 215021, China. E-mail: wlwang@suda.edu.cn*

[d] *National Engineering Laboratory for Modern Silk, Suzhou, 215123, China*

† Electronic supplementary information (ESI) available: Optical images of imprint Si mold and the USP setup, SEM images of FTO tubular arrays after different spray times, surface area calculation and surface area enhancement, EDX of FTO tubular arrays before and after electrodeposition, Raman, FTIR, XRD spectra for material characterization, CV, GCD, gravimetric capacitance, volumetric capacitance and areal capacitance calculation, and optical images of the electrode after the cyclic test. See DOI: 10.1039/c6nr03337g

(ii) an ordered tubular structure with a uniform pore size can help to improve accessibility of the electrolyte to electrodes and thus favors fast ion diffusion and electron transport;[33,34] (iii) pseudocapacitive material deposited on 3-D nanostructures can withstand more volumetric expansion during the electrochemical reaction as 3-D structures can help to release mechanical stress.[33,34] These features bring in synergic improvement of electrode performance based on the combination of effective nanostructures and pseudocapacitive materials.[18]

There are a number of different approaches to fabricate tubular structures, such as top-down lithographic methods and bottom-up self-organized approaches. Top-down approaches are typically expensive and have limited scalability. Meanwhile, bottom-up approaches in principle are much more cost-effective. Among various types of bottom-up approaches, anodization of valve metals, including aluminum (Al), titanium (Ti), *etc.*, can lead to the formation of highly packed oxide nanotubular structures *via* self-organizing mechanisms,[25,35,36] and this approach has been proven highly scalable with cost-effectiveness.[37] In this work, anodic aluminum oxide (AAO) membranes with highly ordered 3-D nanotube arrays were fabricated by a nanoimprint process in conjunction with electrochemical anodization. And the membranes were then utilized to fabricate high performance pseudocapacitors. Such an architecture has a fairly large surface area which can benefit the performance of the devices. It is known that an AAO is not conductive by itself, and therefore a low-cost ultrasonic spray pyrolysis (USP) process was utilized to deposit conductive fluorine doped tin oxide (FTO) tubular structured electrodes inside AAO pores. In this case, the FTO tubes have a highly uniform side wall thickness which can be precisely controlled under spraying conditions. The tubular FTO electrodes are mechanically robust due to the support of the AAO scaffold. And a 20 μm thick structure has 51.8 times surface area of that of a planar electrode with the same projected area. In this work manganese dioxide (MnO_2) was chosen as the pseudocapacitive material deposited on FTO electrodes to demonstrate the device concept due to the fact that it has the advantages of high theoretical specific capacitance (~1370 F g^{-1}), low cost (less than one dollar per pound for the metal), environmentally friendly, *etc*. This material has been widely used as a pseudocapacitive material for many supercapacitor devices.[2] In addition, MnO_2 nanoflakes were electrochemically deposited on the internal surface of FTO tubular electrodes forming a unique hierarchical tubular pseudocapacitor device structure which further enlarges the electrode surface area for more ion diffusion and redox reaction. And thus, the electrode has a high volumetric capacitance of 112.6 F cm^{-3} (10 μm thick AAO) and areal capacitance of 193.8 mF cm^{-2} (20 μm electrode) respectively. This areal capacitance is 18.5 times that of a planar FTO substrate. These results have shown that such a low cost spray process is highly promising for practical fabrication of effective nanostructures to obtain high performance pseudocapacitors.

Results and discussion

The fabrication process of the hierarchical nanotube pseudocapacitive electrodes mainly comprises 4 steps as shown in Fig. 1: (i) nanoimprint on an Al foil to leave ordered indentation (Fig. 1a); (ii) electrochemical anodization to form an AAO membrane with perfect hexagonal ordering (Fig. 1b); (iii) conformal and uniform deposition of FTO tubular structures into AAO nanochannels with the USP method (Fig. 1c); and (iv) homogeneous electrodeposition of MnO_2 nanoflakes into FTO tubular arrays to achieve hierarchical electrodes (Fig. 1d). Optical images of electrodes after different fabrication steps could be found in Fig. S1a.† It is worth mentioning that to form conductive nanotubular structures, atomic layer deposition (ALD) and physical vapor deposition (PVD) methods have been mostly adopted in the past.[19,21,22,28] However, the PVD method is not suitable for long channel high aspect ratio structure deposition due to directionality of the vapor molecules. And the rather high cost and slow deposition rate of ALD also limits its application for practical devices. By contrast, in such a fabrication scheme, the USP process is simply conducted under atmospheric pressure in a fume-hood (Fig. S1b†), and the process is not only of low-cost, but also suitable for conformal deposition of materials in a high aspect ratio structure.

Fig. 2a–f show the optical image and scanning electron microscopy (SEM) images of 10 μm depth freestanding AAO tubular arrays before and after FTO deposition. Obviously, the color of the AAO backbone has been changed from transparent to homogeneous brown, proving the deposition of FTO inside AAO channels and the dense FTO film is conformally and uniformly deposited on the AAO scaffolds, which can be seen in Fig. 2e and f. Fig. 2g shows the FTO tube inner diameter and

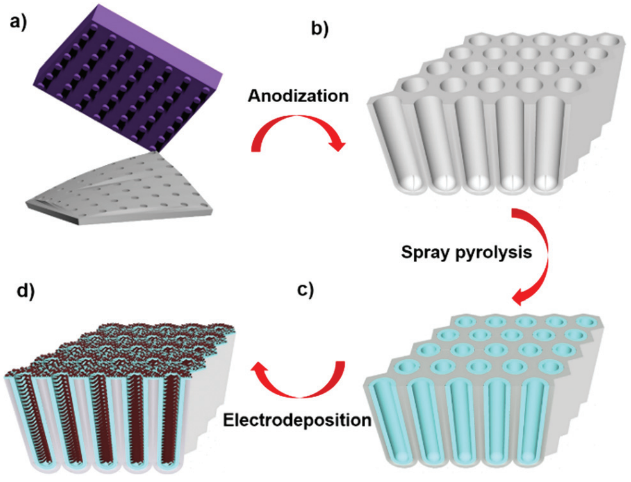

Fig. 1 Schematic illustration showing the fabrication process of hierarchical tubular pseudocapacitor electrodes. (a) Nanoimprint process with hexagonal nanopillar Si mold. (b) As-prepared AAO membranes after anodization and Al removal. (c) USP deposition of FTO tubular arrays. (d) Hierarchical tubular electrodes achieved by MnO_2 electrodeposition.

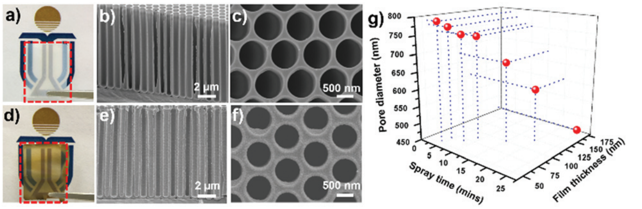

Fig. 2 Optical and SEM images of freestanding AAO tubular arrays with the length of 10 μm before USP (a–c). Optical and SEM images of freestanding AAO tubular arrays with the length of 10 μm after USP (d–f). (g) Pore diameter and film thickness as the functions of USP time.

film thickness as the functions of spray time, with the AAO initial pore diameter of 900 nm (Fig. 2c). The FTO tube inner diameter decreases at the average rate of 11 nm min^{-1} during the USP deposition process, simultaneously with the increasing thickness of the FTO film at the average deposition rate of 5.2 nm min^{-1} (Fig. S2a†). Such a good linear relationship with the spray time demonstrates the precise controllability of the USP deposition method. To further confirm this, the same process was repeated on the 20 μm depth AAO tubular arrays. In these samples, the thickness of the FTO film increases at the average deposition rate of 7.8 nm min^{-1}, while the FTO inner diameter decreases at the average rate of 15.8 nm min^{-1} (Fig. S2b and c†). For applications such as pseudocapacitor electrodes, a naturally large surface area is preferred to accommodate more active material. To attain a large surface area, the pore size was enlarged to 900 nm by wet etching which is already 90% of the periodicity, and a layer of FTO with the thickness of around 100 nm was deposited into both 10 μm and 20 μm AAO tubular arrays. Without removing the AAO scaffold, the highly ordered structural integrity is well maintained addressing the nanostructure collapse issue in some other reports.[8,34] And the corresponding surface area enhancement is nearly 26.4 (10 μm) and 51.8 times (20 μm) that of the planar structure. The detailed calculation method could be seen from Fig. S3a and b.†

In order to realize hierarchical tubular structured pseudocapacitor electrodes, MnO_2 was deposited into the FTO tubular arrays with pulse electrochemical deposition. To obtain the optimized performance, a systematic study was conducted on 10 μm depth FTO tubular arrays *via* controlling the deposition time. Fig. 3a–d show the cross-sectional view and top view SEM images of the structures after different deposition times of 45 s, 60 s, 75 s and 90 s, respectively. Interestingly, it was found that MnO_2 nanoflakes rather than a thin film were uniformly deposited onto the inner side wall of FTO tubular arrays. The interleaved morphology of MnO_2 nanoflakes together with FTO form the hierarchical tubular pseudocapacitor electrodes, and such electrodes could further enhance the surface area for more ion contact and facilitate ion transport vertically along the channels together with horizontal transport along the nanoflake surface. Nevertheless, it can also be seen that the channel diameter becomes smaller and smaller as the amount of MnO_2 increases and it is nearly closed after 90 s electrodeposition (insert in Fig. 3d), leaving the surface a non-ordered structure (Fig. 3d). Such a random structure generates large ion transport resistance, which prevents ions from diffusing into deep channels, and thus leading to poor rate capability.[34] X-ray photoelectron spectroscopy (XPS) of the as-built hierarchical tubular electrode is shown in Fig. 3e. Six elements (Sn, Mn, Al, C, O, and F) are identified at the surface of the electrode. The appearance of Sn, Al and F is attributed to the AAO backbone and FTO conductive layer. Mn stems from MnO_2 achieved by electrodeposition. The trace of O mainly occurs from metal oxide, and C together with the rest of O from adventitious contamination. According to Fig. 3e, two peaks at 641.9 eV and 653.7 eV can be identified, which indicates that the Mn^{4+} ions are dominant in the deposited material. The detailed chemical composition of hierarchical tubular electrodes was probed by using an energy dispersive spectrometer (EDS), shown in Fig. S4.† Different methods for material characterization are shown in Fig. S9.† According to the Raman spectrum shown in Fig. S9a,† a sharp peak located at 650 cm^{-1} proves the existence of MnO_2, which is attributed to the stretching vibration of MnO_6 octahedral molecules. Fourier transform infrared spectroscopy (FTIR) results are shown in Fig. S9b.† The lack of a strong absorption peak at the wavenumber of 3500 cm^{-1} proves that most of the pseudocapacitive materials originate from metal oxide instead of metal hydroxide. X-ray diffraction (XRD) measurement was based on material components of the entire pseudocapacitor electrode

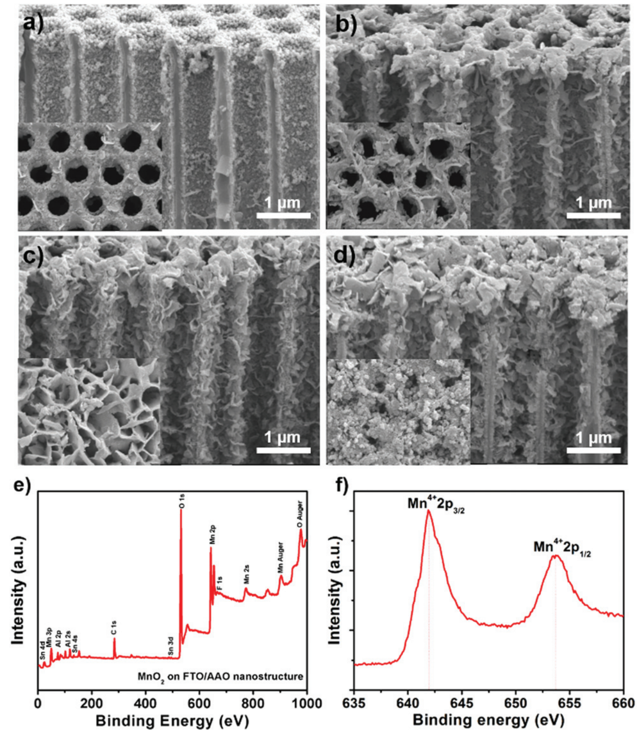

Fig. 3 SEM images of hierarchical tubular electrodes (10 μm length) at different electrodeposition times: (a) 45 s, (b) 60 s, (c) 75 s and (d) 90 s. (e) XPS spectrum of hierarchical tubular electrode and (f) Mn 2p level characterization.

to investigate the crystallographic structure of the materials, which can be seen in Fig. S9c.†

To evaluate the electrochemical performance of the hierarchical tubular electrodes, cyclic voltammetry (CV) measurements with a three-electrode configuration on the as-prepared electrode with a 0.6 cm × 0.5 cm footprint area were conducted in a 1 M Na_2SO_4 liquid electrolyte with voltage ranging from 0 to 0.8 V. In such a configuration, MnO_2 decorated FTO tubular arrays were defined as working electrodes, saturated Ag/AgCl served as a reference electrode and the carbon rod served as a counter electrode. The distance of the neighbouring electrode was 3 cm. Fig. 4a presents the typical CV curves at the scan rate of 50 mV s^{-1} after different electrodeposition times. The much more rectangular shape and larger area enclosed by CV curves demonstrate that the optimized capacitance could be achieved after 75 s electrodeposition. Note that volumetric capacitance and gravimetric capacitance are both important figure-of-merits of a pseudocapacitor, and they can be calculated by using the following equations:

$$C_v = \int_0^{0.8} \left(\left|I_{FTO/MnO_2}\right| - \left|I_{FTO}\right|\right) dU / 2V_0 \Delta U \nu_0 \tag{1}$$

$$C_v = it/\Delta U V_0 \tag{2}$$

$$C_g = \int_0^{0.8} \left(\left|I_{FTO/MnO_2}\right| - \left|I_{FTO}\right|\right) dU / 2m \Delta U \nu_0 \tag{3}$$

$$C_g = it/\Delta U m \tag{4}$$

$$m = QM/2eN_A \tag{5}$$

where C_v and C_g are the volumetric capacitance and gravimetric capacitance of the hierarchical tubular pseudocapacitive electrode, respectively. m and V_0 are the mass of MnO_2 and the volume of the entire electrode including the AAO scaffold. I is the electrical current driven by voltage, i is the discharge current, U is the voltage, ΔU is the operating voltage window (0.8 V), and ν_0 is the scan rate. Q is the amount of charge passing through the entire electrode, M is the molecular weight of MnO_2, e is the electronic charge, and N_A is the Avogadro's number. Note that the mass loading of MnO_2 after 45 s, 60 s, 75 s, and 90 s electrodeposition is 0.151 mg cm^{-2}, 0.201 mg cm^{-2}, 0.251 mg cm^{-2}, and 0.301 mg cm^{-2} respectively, normalized to the projected area of the electrode. Fig. 4b shows the volumetric capacitance and gravimetric capacitance of hierarchical tubular electrodes at the scan rate of 5 mV s^{-1} as functions of electrodeposition time. The peak value of volumetric capacitance can be achieved from the device with 75 s MnO_2 electrochemical deposition, while longer and shorter deposition times both show lower volumetric capacitance. This is due to the fact that volumetric capacitance is normalized to the volume of the entire electrode, augment of MnO_2 mass loading by prolonging deposition time increases overall capacitance. However, excessively long deposition time leads to closing of ion transportation channels, as shown in Fig. 3d, and this causes loss of overall capacitance. As for gravimetric capacitance, it monotonically decreases when increasing deposition time as shown in Fig. 4b. This is because gravimetric capacitance is normalized to the net MnO_2 mass loading, normally more mass loading increases the material thickness that slows down charge transport inside MnO_2 material since it has poor charge mobility. In theory, a thinner layer of MnO_2 can lead to higher gravimetric capacitance, as reported in a number of previous literature studies.[8,20,33] However from a practical standpoint, it is more meaningful to normalize the capacitance with the total electrode or device volume and/or weight,[1,38] and such performances are plotted in Fig. S5a and b.† Obviously, both the highest new gravimetric capacitance and volumetric capacitance were achieved after 75 s deposition, proving the optimized material thickness. Fig. 4c shows the CV curves of an electrode with 75 s MnO_2 deposition at different scan rates. The quasi-rectangular shape with a nearly mirror image of current at the increasing scan rate further confirms that 75 s deposition of MnO_2 on such a three-dimensional structure leads to an excellent pseudocapacitive performance. Basically, no obvious redox peak could be observed for MnO_2 pseudocapacitors because of the continuous redox reaction between Mn(III) and Mn(IV),[2] and we attributed the obvious redox peak occurred in this work to the incomplete redox reaction between MnO_2 and metal ions. The CV curves of electrodes with 30 s, 45 s, and 90 s MnO_2 deposition times at different scan rates are plotted in Fig. S7a–c.† The volumetric capacitance and gravimetric capacitance for 75 s deposition as the functions of scan rate are plotted in Fig. 4d. The highest specific capacitances are 112.6 F cm^{-3} and 449.5 F g^{-1} at the scan rate of 5 mV s^{-1} and the corresponding values are 108.8 F cm^{-3} and 434.3 F g^{-1} at the discharge current density of 0.6 mA cm^{-2}. To further study the composition of total capacitance, CV and galvanostatic charge–discharge (GCD) characterization were also performed

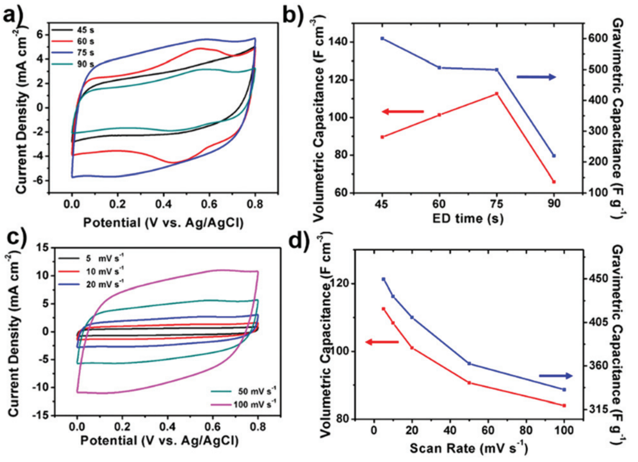

Fig. 4 (a) CV curve of 10 μm hierarchical tubular electrodes after different electrodeposition times at the scan rate of 50 mV s^{-1}. (b) Volumetric capacitance and gravimetric capacitance of 10 μm hierarchical tubular electrodes as the functions of electrodeposition time at the scan rate of 5 mV s^{-1}. (c) CV curves of different scan rates after 75 s electrodeposition. (d) Volumetric capacitance and gravimetric capacitance of 75 s electrodeposition as the functions of the scan rate.

based on 10 μm bare FTO and pseudocapacitor electrodes with 75 s deposition, which are shown in Fig. S6.† The negligible electrical double layer capacitance, around 1.5 mF cm^{-2} at the discharge current density of 0.6 mA cm^{-2}, comes from bare FTO demonstrates little effect on the total capacitance. The areal capacitance, gravimetric capacitance, volumetric capacitance of different deposition times at different scan rates are also shown in Fig. S7d–f.†

To further explore the practical merit of such hierarchical tubular electrodes, 75 s MnO_2 electrodeposition at the same current density was conducted on 3-D FTO tube arrays with 20 μm depth, and the SEM images are shown in Fig. S8a and b.† In order to further show the advantage of hierarchical tubular electrodes, MnO_2 was also deposited onto a planar glass substrate deposited with an FTO film, serving as a control sample for comparison. For the sake of a fair comparison, the amount of MnO_2 was the same compared with that on a 20 μm hierarchical tubular electrode. Fig. 5a presents the CV curve of different electrodes at the scan rate of 5 mV s^{-1}. The largest area surrounded by the CV curve shows that the 20 μm hierarchical tubular electrode has the highest capacitance. By contrast, the irregular shape and smallest area enclosed by the CV curve based on a planar electrode demonstrate the poor pseudocapacitive behavior. GCD characteristics at the current density of 0.6 mA cm^{-2} based on different architectures are also plotted in Fig. 5b. Notably, the longest discharge time of the 20 μm hierarchical tubular electrode demonstrates more charge stored in the electrode with a more complete redox reaction for the active material on the surface. Such results could be rationalized by considering the fact that the nanostructured electrodes always achieve thinner MnO_2 deposition on the surface compared to the planar control sample with the same MnO_2 mass loading due to a much larger surface area, therefore, both the ion diffusion length and electron transport length are much shortened, leading to the lowered resistance for charge transport. GCD based on 10 μm and 20 μm hierarchical tubular electrodes at different current densities are plotted in Fig. S10a and b.† Fig. 5c shows the areal capacitance of different electrodes. It is worth mentioning that the 20 μm hierarchical tubular electrode achieved an areal capacitance of 193.8 mF cm^{-2} at the scan rate of 5 mV s^{-1} and 184 mF cm^{-2} at the discharge current density of 0.6 mA cm^{-2}, however, only 10.6 mF cm^{-2} was obtained from the planar electrode, nearly 18.5 times of the performance enhancement factor was achieved even though they had the same MnO_2 mass loading. The little mismatched enhancement between the surface area and electrochemical performance could result from the difficulty in the ion diffusion caused by channel narrowing down after electrodeposition. And this enhancement factor is nearly 4.3 times that of our previously reported results on nanospike electrodes.[20] Note that we avoid the use of volumetric capacitance for comparison between the hierarchical tubular electrodes and planar electrodes, as the latter is fabricated on a thick glass supporting substrate; it is not a fair comparison if the capacitance is normalized to the entire electrode including the glass substrate. In terms of volumetric capacitance, the 20 μm electrode achieved 96.9 F cm^{-3} at the scan rate of 5 mV s^{-1} and 92 F cm^{-3} at the discharge current density of 0.6 mA cm^{-2} (Fig. S10c and d†), which is slightly lower than that of the 10 μm electrode (112.6 F cm^{-3}). Such a result could be attributed to the larger series resistance along FTO nanotubes when the channel length of the electrode increases, and also the longer ion diffusion time in deeper channels. Typically, obtaining higher areal capacitance can lead to occupying a larger electrode volume and thus, there is a trade off between high areal capacitance and volumetric capacitance. In this work, we have successfully achieved respectably high values on both capacitances, and these values are significantly higher than many previously reported results,[20,24,27,29,39,40] as shown in Fig. 5d.

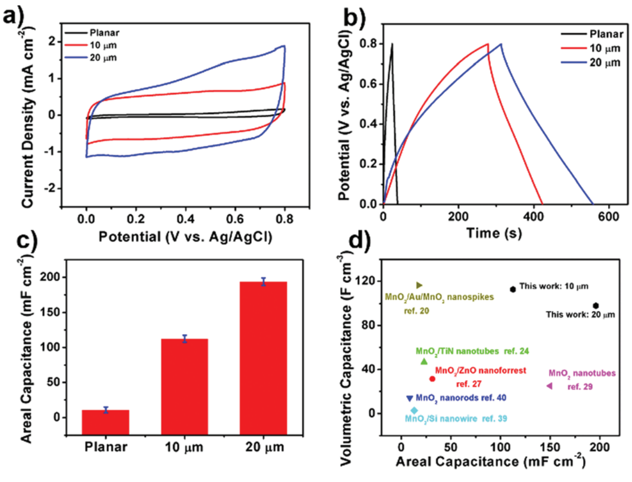

Fig. 5 (a) CV comparison among the planar electrode, 10 μm hierarchical tubular electrode and 20 μm hierarchical tubular electrode at the scan rate of 5 mV s^{-1}. (b) GCD comparison among the planar electrode, 10 μm hierarchical tubular electrode, and 20 μm hierarchical tubular electrode at the current density of 0.6 mA cm^{-2}. (c) Areal capacitance comparison among the planar electrode, 10 μm hierarchical tubular electrode, and 20 μm hierarchical tubular electrode at the scan rate of 5 mV s^{-1} with the error bars. (d) Volumetric capacitance as the function of areal capacitance for different nanostructured electrodes.

To further examine the electrochemical performance of the hierarchical structured electrode, electrochemical impedance spectroscopy (EIS) measurements were conducted in the frequency range from 100 kHz to 0.01 Hz and the result is shown in Fig. 6a. It is clearly seen that the planar electrode has the largest radius for the semicircle in the high frequency range (insert in Fig. 6a), which reflects the largest charge-transfer resistance compared with nanostructured hierarchical tubular electrodes. Moreover, the linear region at the low frequency region is controlled by the Warburg impedance, defined as the diffusion resistance of the metal alkali ions. The intersection of the X axis and the reversed extension line at the low frequency reflects the value of the Warburg coefficient (σ), and such a value is directly proportional to the Warburg impedance (R_w). In this manner, the larger portion of the Warburg impedance region at the low frequency further demonstrates

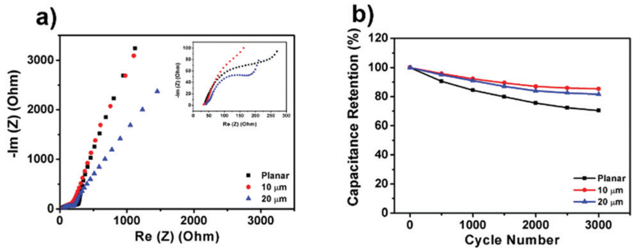

Fig. 6 (a) Nyquist plots of the planar electrode, 10 μm hierarchical tubular electrode, and 20 μm hierarchical tubular electrode. (b) Cycling performance of the planar electrode, 10 μm hierarchical tubular electrode, and 20 μm hierarchical tubular electrode during 3000 cycles at the scan rate of 100 mV s^{-1}.

that the planar electrode hinders the diffusion of the ions. In addition, the linear region at the low frequency could also be regarded as the semi-infinite diffusion model, and the slightly deviated value for the slope from 1 is because the reaction occurs at the electrode surface which is not merely controlled by electrode potential but also other state variables. The cyclic stability test was also conducted on both nanostructured and planar electrodes at the scan rate of 100 mV s^{-1}, which could be seen in Fig. 6b. Specifically, 85.4% and 81.6% capacitance retentions were achieved for 10 μm and 20 μm hierarchical tubular electrodes after 3000 cycles of test. However, it is only 70.3% for the planar electrode, and such a result could be explained by the charge storage mechanism in pseudocapacitive materials. The charge storage process mainly consists of (i) a surface redox reaction and (ii) intercalation of ions in the bulk materials,[34] which could be described according to the following formulae:

$$\mathrm{MnO}_{2(\mathrm{surface})} + \mathrm{X}^+ + \mathrm{e}^- \rightleftharpoons \mathrm{MnOOX}_{(\mathrm{surface})} \quad (6)$$

$$\mathrm{MnO}_{2(\mathrm{bulk})} + \mathrm{X}^+ + \mathrm{e}^- \rightleftharpoons \mathrm{MnOOX}_{(\mathrm{bulk})} \quad (7)$$

where X^+ refers to cations in the electrolyte, such as Li^+, Na^+, *etc*. The volumetric expansion during the test compromised the performance stability of the planar electrode, and after hundreds of cycles, MnO_2 was exfoliated from the planar substrate, which could be seen in Fig. S11a and b.† However, a nanostructure based electrode could withstand more volume expansion due to the anchor effect protection from the 3D backbones, and thus showing more stable capacitance retention (Fig. S11c and d†).

The symmetric pseudocapacitor device was further fabricated to elucidate the advantages of such a hierarchical structure. The CV curve and GCD are plotted in Fig. 7a and b. The highest areal capacitance and volumetric capacitance for the device occur at the discharge current density of 0.1 mA cm^{-2} and the corresponding performances are 87.4 mF cm^{-2} and 17.5 F cm^{-3}, respectively. Note that the volume of the total device includes two pseudocapacitor electrodes with the same thickness of 20 μm and a separator with the thickness of 10 μm and the solid state electrolyte. For practical application, specific energy and specific power are the two pivotal benchmarks for pseudocapacitors, which could be calculated from the following equations:

$$E = C_{\mathrm{v}}(\Delta E)^2/2 \quad (8)$$

$$P = (\Delta E)^2/4RV \quad (9)$$

$$R = U_{\mathrm{drop}}/2i \quad (10)$$

where E and P are the specific energy and specific power of the device. ΔE is the voltage window of the device excluding the voltage drop (U_{drop}), V is the volume of the total device, and R is the internal resistance of the device. The Ragone plot is shown in Fig. 7d and the highest specific energy is 1.56 × 10^{-3} Wh cm^{-3} with the corresponding specific power value of 14.2 W cm^{-3}, and such performances are superior to many previous reports.[6,17,20,30,41,42] Moreover, the cyclic stability of the pseudocapacitor device was also tested at the scan rate of 100 mV s^{-1}, which is shown in Fig. S12.† It is worth mentioning that the capacitance still maintains 80% of its initial value after 5000 cycles, and thus demonstrating the reliable pseudocapacitive behavior of such hierarchical structures.

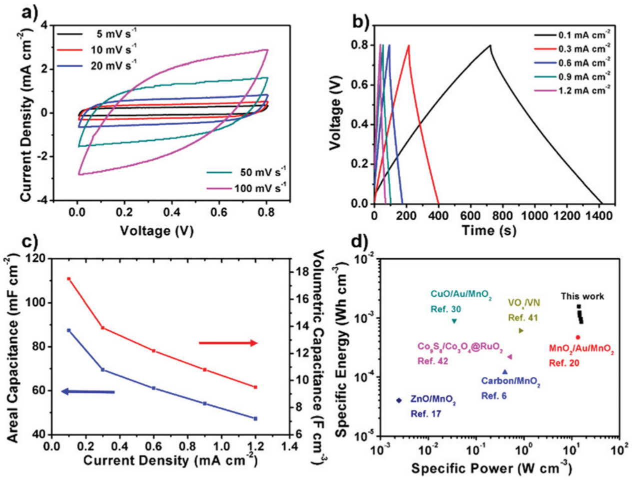

Fig. 7 (a) CV curves of symmetric supercapacitors at different scan rates. (b) GCD curve of the symmetric supercapacitor device with different current densities. (c) Areal capacitance and volumetric capacitance of the supercapacitor device calculated based on different current densities. (d) Ragone plot shows the specific energy and specific power of the device.

Conclusions

Herein, we report a three-dimensional hierarchical structure which consists of nanotubular FTO and MnO_2 nanoflakes deposited inside the FTO nanotubes for high performance pseudocapacitors. The entire electrode structure was fabricated on an anodic aluminum oxide template with a large pore diameter. The FTO nanotube electrodes were fabricated with a cost-effective USP process without removing the AAO scaffold and thus the structural integrity was well maintained. It was discovered that a nanotubular electrode has 51.8 times of the surface area compared to a planar electrode. Thus the hierarchical structured electrodes demonstrated a volumetric capacitance of 112.6 F cm^{-3} normalized to the entire electrode volume, and an areal capacitance of 193.8 mF cm^{-2} normalized to the electrode projected area. The unique hierarchical structure leads to a remarkable enhancement in the pseudocapacitive capacitance of 18.5 times over a planar electrode with the same MnO_2 mass loading. The marginal change of the capacitance after the cyclic test further shows that such electrodes are highly robust. In addition, the pseudocapacitor device fabricated based on such electrodes achieves a high volumetric capacitance of 17.5 F cm^{-3}, together with the highest specific energy of 1.56×10^{-3} Wh cm^{-3}. With the merits of low cost fabrication procedures and enhanced electrochemical performance, such three-dimensional hierarchical tubular electrodes are attractive for high performance electrical energy storage devices.

Experimental section

Preparation of AAO tubes

Aluminum foil with the thickness of 0.25 mm and area of 3 cm × 2 cm was prepared by cutting, followed by electrochemically cleaning under 12 V constant voltage for 2 min. After that, 5 mm × 5 mm silicon stamps with ordered hexagonal nanopillars with the height of 0.1 μm and pitch of 1 μm were utilized as imprinting mold to produce a nanoindentation array on the surface of the as-prepared aluminum foil. Afterwards, the aluminum foil undergoes one-step anodization for AAO tubes of 10 μm and 20 μm under 400 V direct voltage. Then, the AAO tubes with the channel length of 10 μm and 20 μm are immersed into the 5 v% H_3PO_4 for 65 min and 70 min, respectively at the temperature of 53 °C to enlarge the pore size. Finally, the Al substrate was removed using saturated mercuric chloride to achieve free-standing AAO tubes.

Preparation of FTO precursor solution

FTO precursor solution was firstly prepared by refluxing. Typically, 21 g $SnCl_4 \cdot 5H_2O$ was added into 300 ml absolute ethanol in a three-necked flask and refluxed for 1 hour with the temperature of 60 °C, with magnetic stirring to form a uniform, stable and transparent solution. Afterwards, 450 mg of NH_4F was then dissolved into 10 ml DI water and added dropwise into the $SnCl_4$/ethanol solution. The refluxing system was maintained for another 3 hours, followed by natural cooling to room temperature.

Fabrication of FTO tubular arrays

A homemade two-terminal USP equipment was used for FTO deposition, as shown in Fig. S1b.† Firstly, AAO samples with the channel length of 10 μm and 20 μm were fixed on a hot plate, and compressed air working as the carry gas was injected into the input terminal of the USP setup. The output terminal was connected with a nozzle which covers AAO substrates. Then the sonicator was turned on to actuate and vaporize the precursor solution. Driven by the compressed air, the vaporized precursor reached the hot surface of AAOs and the FTO tubular structure was formed when the pyrolysis reaction occurred. The deposition process is conducted under the temperature of 400 °C and for different times. After finishing FTO deposition, the samples are annealed under an Ar atmosphere for 2 hours with the temperature of 500 °C, followed by naturally cooling to room temperature.

Fabrication of hierarchical tubular electrodes

FTO tubular arrays with the channel length of 10 μm are used for systematic study of the electrochemical performance of the hierarchical tubular electrode. A galvanostatic square waveform with a duty cycle of 1% and frequency of 1 Hz was applied for pulsed electrochemical deposition. Different amounts of MnO_2 were electrochemically deposited by precise control of the cycles from 4500 to 9000 with the constant current of 6.67 mA for the projected 1 cm^2 at room temperature. Later, the same electrodeposition process was conducted based on planar structure and 20 μm FTO tubular arrays and the amount of MnO_2 was doubled compared with 10 μm hierarchical tubular arrays. The deposition solution consists of 0.05 M manganese acetate ($MnAc_2$), 98% purity and 0.1 M sodium sulfate (Na_2SO_4), 99% purity.

Characterization of samples

Various analytical techniques were utilized to characterize the as-fabricated nanostructured electrode. Morphologies were characterized using field-emission scanning electron microscopy (JSM-7100F, Japan). Chemical compositions were studied by X-ray photoelectron spectroscopy (PHI 5600, USA) and using an energy dispersive spectrometer (JSM-7100F, Japan). CV, GCD and EIS measurements based on a three-electrode configuration were performed on an electrochemical workstation (Gamry, USA). CV was carried out at different scan rates of 5, 10, 20, 50, and 100 mV s^{-1}. GCD was measured at 0.6, 1.2, 1.8, 2.4, and 3.6 mA cm^{-2}. EIS was measured with the frequency range from 100 kHz to 0.01 Hz with a potential amplitude of 10 mV.

Acknowledgements

The authors thank Mr H. Y. Jin from the Department of Applied Physics, The Hong Kong Polytechnic University for their helpful discussion. The authors also thank Mrs Y. Zhang and Mr Alex HK Wong from Materials Characterization and Preparation Facility (MCPF), The Hong Kong University of Science and Technology for their help in SEM analysis. The work was supported by the General Research Fund (project 612113) from the Hong Kong Research Grant Council and the Hong Kong Innovation and Technology Fund (project ITS/117/13, ITS/362/14FP) from the Innovation and Technology Commission, Hong Kong SAR and the Priority Academic Program Development of Jiangsu Higher Education Institutions (PAPD).

Notes and references

1 J. R. Miller and P. Simon, *Sci. Mag.*, 2008, **321**, 651–652.

2 P. Simon and Y. Gogotsi, *Nat. Mater.*, 2008, **7**, 845–854.

3 X. Wang, X. Lu, B. Liu, D. Chen, Y. Tong and G. Shen, *Adv. Mater.*, 2014, **26**, 4763–4782.

4 Y. Gogotsi, *Nature*, 2014, **509**, 568–570.

5 X. Xia, Y. Zhang, D. Chao, C. Guan, Y. Zhang, L. Li, X. Ge, I. M. Bacho, J. Tu and H. J. Fan, *Nanoscale*, 2014, **6**, 5008–5048.

6 X. Xiao, T. Li, P. Yang, Y. Gao, H. Jin, W. Ni, W. Zhan, X. Zhang, Y. Cao and J. Zhong, *ACS Nano*, 2012, **6**, 9200–9206.

7 R. Yi, S. Chen, J. Song, M. L. Gordin, A. Manivannan and D. Wang, *Adv. Funct. Mater.*, 2014, **24**, 7433–7439.

8 Z. Yu, B. Duong, D. Abbitt and J. Thomas, *Adv. Mater.*, 2013, **25**, 3302–3306.

9 M. Zhi, C. Xiang, J. Li, M. Li and N. Wu, *Nanoscale*, 2013, **5**, 72–88.

10 M. Huang, F. Li, F. Dong, Y. X. Zhang and L. L. Zhang, *J. Mater. Chem. A*, 2015, **3**, 21380–21423.

11 D. N. Futaba, K. Hata, T. Yamada, T. Hiraoka, Y. Hayamizu, Y. Kakudate, O. Tanaike, H. Hatori, M. Yumura and S. Iijima, *Nat. Mater.*, 2006, **5**, 987–994.

12 X. Lu, M. Yu, G. Wang, T. Zhai, S. Xie, Y. Ling, Y. Tong and Y. Li, *Adv. Mater.*, 2013, **25**, 267–272.

13 D. Pech, M. Brunet, H. Durou, P. Huang, V. Mochalin, Y. Gogotsi, P. Taberna and P. Simon, *Nat. Nanotechnol.*, 2010, **5**, 651–654.

14 A. L. M. Reddy, S. R. Gowda, M. M. Shaijumon and P. M. Ajayan, *Adv. Mater.*, 2012, **24**, 5045–5064.

15 X. Xia, D. Chao, Z. Fan, C. Guan, X. Cao, H. Zhang and H. J. Fan, *Nano Lett.*, 2014, **14**, 1651–1658.

16 X. Xia, Y. Zhang, Z. Fan, D. Chao, Q. Xiong, J. Tu, H. Zhang and H. J. Fan, *Adv. Energy Mater.*, 2015, **5**(6), 1401709.

17 P. Yang, X. Xiao, Y. Li, Y. Ding, P. Qiang, X. Tan, W. Mai, Z. Lin, W. Wu and T. Li, *ACS Nano*, 2013, **7**, 2617–2626.

18 Z. Yu, L. Tetard, L. Zhai and J. Thomas, *Energy Environ. Sci.*, 2015, **8**, 702–730.

19 X. Chen, E. Pomerantseva, P. Banerjee, K. Gregorczyk, R. Ghodssi and G. Rubloff, *Chem. Mater.*, 2012, **24**, 1255–1261.

20 Y. Gao, H. Jin, Q. Lin, X. Li, M. M. Tavakoli, S. Leung, W. M. Tang, L. Zhou, H. L. W. Chan and Z. Fan, *J. Mater. Chem. A*, 2015, **3**, 10199–10204.

21 F. Grote and Y. Lei, *Nano Energy*, 2014, **10**, 63–70.

22 F. Grote, L. Wen and Y. Lei, *J. Power Sources*, 2014, **256**, 37–42.

23 U. N. Maiti, J. Lim, K. E. Lee, W. J. Lee and S. O. Kim, *Adv. Mater.*, 2014, **26**, 615–619.

24 S. A. Sherrill, J. Duay, Z. Gui, P. Banerjee, G. W. Rubloff and S. B. Lee, *Phys. Chem. Chem. Phys.*, 2011, **13**, 15221–15226.

25 Y. Song, Y. Li, J. Guo, Z. Gao and Y. Li, *J. Mater. Chem. A*, 2015, **3**(47), 23754–23759.

26 Z. Su, C. Yang, B. Xie, Z. Lin, Z. Zhang, J. Liu, B. Li, F. Kang and C. Wong, *Energy Environ. Sci.*, 2014, **7**(8), 2652–2659.

27 X. Sun, Q. Li, Y. Lü and Y. Mao, *Chem. Commun.*, 2013, **49**, 4456–4458.

28 L. Wen, Y. Mi, C. Wang, Y. Fang, F. Grote, H. Zhao, M. Zhou and Y. Lei, *Small*, 2014, **10**, 3162–3168.

29 H. Xia, J. Feng, H. Wang, M. O. Lai and L. Lu, *J. Power Sources*, 2010, **195**, 4410–4413.

30 Z. Yu and J. Thomas, *Adv. Mater.*, 2014, **26**, 4279–4285.

31 Z. Yu, C. Li, D. Abbitt and J. Thomas, *J. Mater. Chem. A*, 2014, **2**, 10923–10929.

32 X. Zhang, X. Peng, W. Li, L. Li, B. Gao, G. Wu, K. Huo and P. K. Chu, *Small*, 2015, **11**, 1847–1856.

33 S. Chabi, C. Peng, D. Hu and Y. Zhu, *Adv. Mater.*, 2014, **26**, 2440–2445.

34 H. Zhao, C. Wang, R. Vellacheri, M. Zhou, Y. Xu, Q. Fu, M. Wu, F. Grote and Y. Lei, *Adv. Mater.*, 2014, **26**, 7654–7659.

35 S. Leung, L. Gu, Q. Zhang, K. Tsui, J. Shieh, C. Shen, T. Hsiao, C. Hsu, L. Lu, D. Li, Q. Lin and Z. Fan, *Sci. Rep.*, 2014, **4**, 4243.

36 Y. Lin, Q. Lin, X. Liu, Y. Gao, J. He, W. Wang and Z. Fan, *Nanoscale Res. Lett.*, 2015, **10**, 495.

37 M. H. Lee, N. Lim, D. J. Ruebusch, A. Jamshidi, R. Kapadia, R. Lee, T. J. Seok, K. Takei, K. Y. Cho and Z. Fan, *Nano Lett.*, 2011, **11**, 3425–3430.

38 Y. Gogotsi and P. Simon, *Sci. Mag.*, 2011, **334**, 917–918.

39 D. P. Dubal, D. Aradilla, G. Bidan, P. Gentile, T. J. Schubert, J. Wimberg, S. Sadki and P. Gomez-Romero, *Sci. Rep.*, 2015, **5**, 9771.

40 S. Santhanagopalan, A. Balram and D. D. Meng, *ACS Nano*, 2013, **7**, 2114–2125.

41 X. Lu, M. Yu, T. Zhai, G. Wang, S. Xie, T. Liu, C. Liang, Y. Tong and Y. Li, *Nano Lett.*, 2013, **13**, 2628–2633.

42 J. Xu, Q. Wang, X. Wang, Q. Xiang, B. Liang, D. Chen and G. Shen, *ACS Nano*, 2013, **7**, 5453–5462.